



# Effect of crystallinity on capacity and cyclic stability of $\text{Na}_{1.1}\text{V}_3\text{O}_{7.9}$ nanoplates as lithium-ion cathode materials

Huifeng Zhuang<sup>1</sup> · Yue Xu<sup>1</sup> · Ping Zhao<sup>1</sup>

Received: 1 October 2019 / Revised: 16 December 2019 / Accepted: 17 December 2019 / Published online: 3 January 2020  
© Springer-Verlag GmbH Germany, part of Springer Nature 2020

## Abstract

High-crystalline  $\text{Na}_{1.1}\text{V}_3\text{O}_{7.9}$  nanoplates were synthesized by a facile sol-gel reaction followed by calcination. The microstructure and crystallinity of the nanoplates were primarily determined by calcination temperature. The maximum crystallinity  $\text{Na}_{1.1}\text{V}_3\text{O}_{7.9}$  sample was calcined at 500 °C was calculated by XRD, and the DSC demonstrated that the amorphous transformation temperature begins at 550 °C. The XPS spectrum confirmed the presence of  $\text{Na}_{1.1}\text{V}_3\text{O}_{7.9}$  and consistent with the XRD test results. The SEM/TEM test illustrated the crystal particle growth of the  $\text{Na}_{1.1}\text{V}_3\text{O}_{7.9}$  nanoplates. Electrochemical results showed that the maximum crystallinity  $\text{Na}_{1.1}\text{V}_3\text{O}_{7.9}$  sample prepared at 500 °C exhibited the optimum performance when evaluated as a cathode material for lithium-ion batteries: the discharge capacity was maintained at 195 mAh  $\text{g}^{-1}$  after 150 cycles at a current of 100 mA  $\text{g}^{-1}$ .

**Keywords** High-crystalline ·  $\text{Na}_{1.1}\text{V}_3\text{O}_{7.9}$  · Cathode materials · Lithium-ion batteries

## Introduction

The popularity of portable electronic digital appliances and electric vehicles is relying on high-performance lithium-ion batteries increasingly [1–6]. However, the cycling performance and energy density of commercial lithium-ion batteries are poor and do not meet the current energy storage requirement. This issue could be addressed by research and development of new cathode materials [7, 8]. In this regard, scholars have focused on developing new electrode materials with high capacity and power density [9–12]. Vanadium-based oxides and vanadates, which exhibit the advantages of high capacity, high energy density, low cost, and abundant resources, have

attracted the interest of researchers and are one of the most studied cathode materials [13–17]. Also, vanadates possess a higher specific capacity than conventional cathode materials ( $\text{LiCoO}_2$  [18],  $\text{LiMn}_2\text{O}_4$  [19–21],  $\text{LiMnO}_2$  [22], and  $\text{LiFePO}_4$  [22–25]) for lithium-ion batteries [26, 27]. However, conventional vanadium-based oxides and vanadates have disadvantages used as a cathode material, such as low lithium-ion diffusion coefficient and poor long-term cycling performance [28]. In particular,  $\text{LiV}_3\text{O}_8$  has gained increasing attention, which has a crystal structure that can accommodate three or more lithium ions and thus has a high reversible theoretical specific capacity [29].  $\text{NaV}_3\text{O}_8$  has the same monoclinic layer structure as  $\text{LiV}_3\text{O}_8$ ; considering that the radius of  $\text{Na}^+$  is larger than that of  $\text{Li}^+$ ,  $\text{NaV}_3\text{O}_8$  has a larger interlayer distance than  $\text{LiV}_3\text{O}_8$ , resulting in easier insertion and extraction of lithium ions [30]. Cao et al. [31] prepared  $\text{NaV}_3\text{O}_8$  nanoplate through in the situ template method and used it as lithium-ion cathode; the cathode exhibited a high reversible capacity of 230 mAh  $\text{g}^{-1}$  and a capacity retention rate of 93.4% after 200 cycles at a current density of 100 mA  $\text{g}^{-1}$ .  $\text{Na}_{1.1}\text{V}_3\text{O}_{7.9}$  (JCPDS No: 45–0498, lattice parameters:  $a = 13 \text{ \AA}$ ,  $b = 8.388 \text{ \AA}$ , and  $c = 14.102 \text{ \AA}$ ,  $\beta = 101.7^\circ$ ) has the same monoclinic structure as  $\text{NaV}_3\text{O}_8$  and layers of mixed V-O octahedral and tetrahedral units forming slabs parallel to (001), and the interlayer space contains sodium and oxygen ions. In this framework, interstitial channels along  $b$ -axes could provide

**Electronic supplementary material** The online version of this article (<https://doi.org/10.1007/s10008-019-04482-4>) contains supplementary material, which is available to authorized users.

- ✉ Yue Xu  
xuyue@qlu.edu.cn
- ✉ Ping Zhao  
zhaoping6101@qlu.edu.cn

<sup>1</sup> Key Laboratory of Processing and Testing Technology of Glass & Functional Ceramics of Shandong Province, School of Material Science and Engineering, Qilu University of Technology (Shandong Academy of Sciences), Jinan 250353, People's Republic of China

large cavities, and the  $\text{Na}^+$  ions in the layer space support two independent positions [32]. Liang et al. [13], synthesized  $\text{Na}_{1.1}\text{V}_3\text{O}_{7.9}$  nanobelts by a facile and scalable hydrothermal reaction followed by calcination; the electrode delivered a high specific capacity of  $204 \text{ mAh g}^{-1}$  at the current density of  $100 \text{ mA g}^{-1}$ . Previous works achieved significant breakthroughs in lithium and sodium batteries; however, the stability of cycle performance has been the bottleneck in the development of layered vanadium-based electrode materials.

In this paper,  $\text{Na}_{1.1}\text{V}_3\text{O}_{7.9}$  electrode was synthesized by a simple method, and the relationship between crystal structure and electrochemical performance was discussed. The crystal structure was studied by XRD and HRTEM tests; DSC and XPS tests have described the transformation of crystal structure also. The SEM/TEM test illustrated the crystal particle growth of the  $\text{Na}_{1.1}\text{V}_3\text{O}_{7.9}$  nanoplates. Electrochemical results show that  $\text{Na}_{1.1}\text{V}_3\text{O}_{7.9}$  exhibits outstanding electrochemical performance and could be a major cathode material for next-generation lithium-ion batteries.

## Experimental section

### Material synthesis

$\text{Na}_{1.1}\text{V}_3\text{O}_{7.9}$  electrode was prepared through a sol-gel method using  $\text{V}_2\text{O}_5$ , oxalic acid, and  $\text{NaNO}_3$  as raw materials (all chemicals were of analytical grade). As shown in Fig. 1, 1.6 g of  $\text{V}_2\text{O}_5$  and 3.327 g of oxalic acid were added into 200 ml of deionized water under stirring at  $80^\circ\text{C}$  for 1 h. The solution was added with 0.548 g of  $\text{NaNO}_3$  as a precursor. The solution was kept at  $100^\circ\text{C}$ . The solvent was evaporated to obtain sol, which was further dehydrated to a dark blue gel. The bright dark blue solid was dried at  $80^\circ\text{C}$  for 12 h, cooled

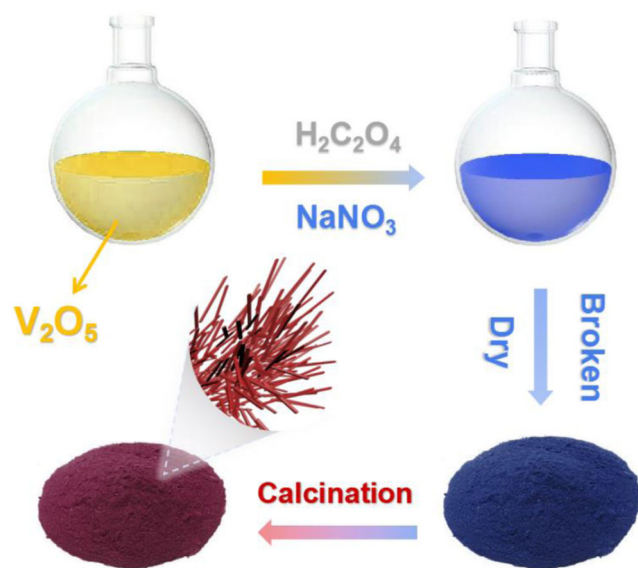


**Fig. 1** Flow chart for the preparation of  $\text{Na}_{1.1}\text{V}_3\text{O}_{7.9}$

naturally, pulverized, and calcined in air at  $350^\circ\text{C}$ ,  $400^\circ\text{C}$ ,  $450^\circ\text{C}$ ,  $500^\circ\text{C}$ , and  $550^\circ\text{C}$  for 4 h. The obtained  $\text{Na}_{1.1}\text{V}_3\text{O}_{7.9}$  products were designated as NVO350, NVO400, NVO450, NVO500, and NVO550.

### Material characterization

Crystal phase composition and crystallinity were examined by X-ray diffraction (XRD, D8-ADVANCE). The diffraction patterns were collected at a scan rate of  $6^\circ$  per min over a diffraction angle of  $2\theta$  range of  $5^\circ$ – $65^\circ$ . The morphologies and sizes of the products were investigated by scanning electron microscopy (SEM, HITACHI, S-4800) and transmission electron microscopy (TEM, Tecnai F30). The sample surface element, valence state, and other information were detected by XPS (Thermo Scientific Escalab 250Xi).

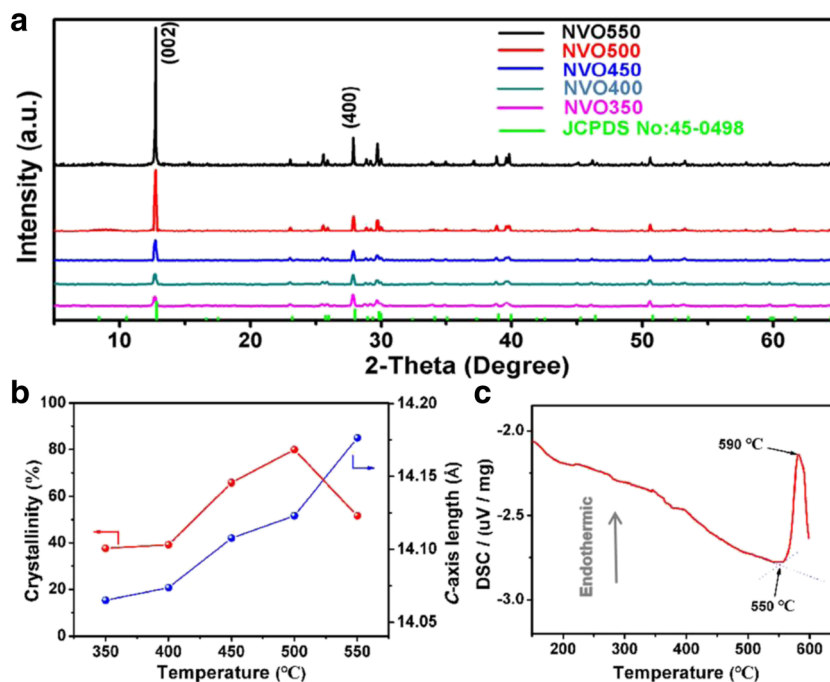
### Electrochemical measurement

Active materials, namely, acetylene black and polyvinylidene fluoride (PVDF), were mixed by the weight ratio of 7:2:1 in N-methyl-2-pyrrolidone (NMP) solution to make a paste. The paste was coated on aluminum foil, dried under an air atmosphere at  $80^\circ\text{C}$  for 10 h and under vacuum atmosphere at  $100^\circ\text{C}$  for 12 h, and cut into circular pieces of 12 mm in diameter. CR2016 coin cells were assembled in a glove box filled with high-purity argon by using metallic lithium and polypropylene film as anode and separator, respectively. The electrolyte was composed of 1 M  $\text{LiPF}_6$  dissolved in ethylene carbonate/dimethyl carbonate/ethylene methyl carbonate (EC/DMC/EMC = 1:1:1, v/v/v). The electrolyte was aged for more than 24 h to ensure cell stability. Galvanostatic charging/discharging tests were conducted using channel battery analyzer (Land CT 2001A, Wuhan, China) within the voltage range of 1.5–4.0 V at different current densities. Cyclic voltammetry (CV) test was performed on an electrochemical workstation (CHI660E, China) at a scan rate of  $0.1 \text{ mV s}^{-1}$  within the voltage range of 1.5–4.0 V. Impedance was recorded within the frequency range of 100 kHz to 10 mHz on a cell in assembled condition.

## Results and discussion

The X-ray diffractograms (XRD) in Fig. 2a suggest that all the as-prepared  $\text{Na}_{1.1}\text{V}_3\text{O}_{7.9}$  samples were monoclinic crystalline structure. The results show that the samples are well converged with the monoclinic P21/m (11) space group (JCPDS card 45–0498). The intensity of the peak corresponding to the (002) plane increases sharply with increasing calcination temperature (match with Table 1). As shown in Fig. 2a, the highest intensity peaks coincide with the (400) plane for the NVO400 sample and (002) plane for the NVO450 and

**Fig. 2** (a) XRD patterns of the as-prepared  $\text{Na}_{1.1}\text{V}_3\text{O}_{7.9}$  samples at different calcination temperature (350 °C, 400 °C, 450 °C, 500 °C, and 550 °C). (b) The crystallinity and  $c$ -axis length of the as-prepared  $\text{Na}_{1.1}\text{V}_3\text{O}_{7.9}$  samples at different temperatures. (c)  $\text{Na}_{1.1}\text{V}_3\text{O}_{7.9}$  sample DSC curve



NVO500 samples. However, the other peaks are substantially unchanged, with the calcination temperature increased. This phenomenon, due to the speed of crystal, grows in the  $c$ -axis direction more than in the other directions with increasing calcination temperature (Table 1). Crystallinity is used to indicate the proportion of crystalline regions in the polymer [33]. For polycrystals, the peak intensity is determined by the number of crystal planes arranged in the same direction. If all the crystal grains are arranged in the same direction, then the peak intensity of each crystal plane is larger than that of the irregularly arranged crystal grains. The different peak intensities in the same spectrum are determined by the number of crystal planes corresponding to each peak. The crystallinity of samples was calculated by the “jade 6.0” software via the relative crystallinity calculation method (Supporting Information). It is known that the  $c$ -axis of the  $\text{Na}_{1.1}\text{V}_3\text{O}_{7.9}$  sample increases as the calcination temperature increases (Table 1), means the crystal grains grow along the  $c$ -axis direction, which indicates that the number of (002) crystal planes increases, and the SEM also proved that the nanoplates have increased (Fig. 4a–c). The crystallinity and orientation of

the crystals are discussed in detail in the supporting information. For the investigation, we tested the  $\text{Na}_{1.1}\text{V}_3\text{O}_{7.9}$  using scanning calorimetry (DSC), because DSC is an important tool for evaluating amorphous phase transitions [34]. The DSC test result was shown in Fig. 2c; the curve has a distinct endothermic peak at 590 °C and the starting inflection point at 550 °C, which means the amorphous transformation begins at 550 °C. Therefore, the sample calcined at 550 °C has an amorphous state, so the crystallinity of the NVO550 sample is lower than that of the NVO500 sample. Combined with the XRD test results (Fig. 2a), there were only one phase when  $\text{Na}_{1.1}\text{V}_3\text{O}_{7.9}$  samples were calcination at different temperatures. XPS test was conducted to obtain important information for exploring the surface molecular and electronic structure and the elemental valence state of the prepared NVO500 samples. As shown in Fig. 3, two well-forming peaks were found at 517.2 and 524.7 eV in the V2p core level spectrum; these peaks are ascribed to the spin-orbit splitting of the components, namely,  $\text{V}2\text{p}_{3/2}$  and  $\text{V}2\text{p}_{1/2}$ , respectively [35]. In Fig. 3, the dominant core level at 517.2 eV is consistent with the literature values for  $\text{V}^{5+}$  ( $\text{V}2\text{p}_{3/2}$ ) in  $\text{V}_2\text{O}_5$  or other vanadates

**Table 1** Lattice parameter and crystallinity of  $\text{Na}_{1.1}\text{V}_3\text{O}_{7.9}$  at different calcination temperatures

Sample	Space group	$a$ (Å)	$b$ (Å)	$c$ (Å)	Crystallinity	Peak area of the (002) plane
NVO350	P21/m(11)	12.7990	8.2116	14.0649	37.61%	2966
NVO400	P21/m(11)	12.7765	8.1971	14.0736	39.16%	3487
NVO450	P21/m(11)	12.8593	8.3884	14.1077	65.77%	4828
NVO500	P21/m(11)	12.9094	8.3803	14.1231	79.92%	12,387
NVO550	P21/m(11)	12.8194	8.2806	14.1764	51.62%	16,429

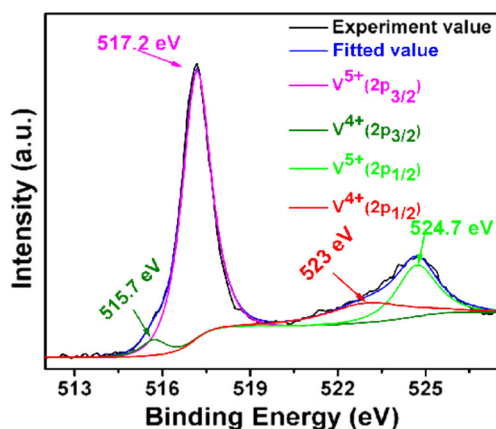


**Fig. 3** XPS spectrum of V 2p of NVO500 sample

[36]. The satellite core level at 515.7 eV with a weak signal is attributed to  $V^{4+}$  ( $V2p_{3/2}$ ) [37]. Also, the satellite core level at 524.7 and 523 eV corresponds to  $V^{5+}$  ( $V2p_{1/2}$ ) and  $V^{4+}$  ( $V2p_{1/2}$ ), respectively [38]. The proportion of  $V^{5+}$  and  $V^{4+}$  is 89.5% and 10.5%, respectively. These results agree well with the presence of  $Na_{1.1}V_3O_{7.9}$ , which is consistent with the XRD test results.

To better observe the micro-morphology of the powder synthesized by calcination at various temperatures from 450 to 550 °C for 4 h, we characterized the topography of the  $Na_{1.1}V_3O_{7.9}$  sample by SEM. As shown in Fig. 4, the effect of calcination temperature on the morphology was significant. In Fig. 4a, the NVO450 sample is composed of nanoplates,

with a thickness of about 100 nm and length of several micrometers. At the calcination temperature of 500 °C (Fig. 4b), the nanoplates become thicker, and the length of nanoplates increases significantly. At the calcination temperature of 550 °C, the nanoplates consist of partial fragments and long micrometer rods with the disordered arrangement (Fig. 4c). As the calcination temperature increases, the size of the sample increases dramatically. The TEM images for the NVO500 samples are recorded in Fig. 4d. The edges of a single nanoplate are stepped, and the crystals grow in a stepwise and layered manner. The growth pattern will result in preferential growth in the direction of the  $c$ -axis, consistent with the XRD results. The HRTEM tests on a single NVO500 sample [Fig. 4 (inset in d)]. The HRTEM images of individual nanoplates show organized lattice fringes with spacings of 0.6 and 0.2 nm, which can be indexed to the (002) and (400) planes of the monoclinic  $Na_{1.1}V_3O_{7.9}$  structure, respectively, consistent with the crystal structure calculations (Fig. 2a). The element distribution mapping test was performed in the area of Fig. 4e, and as shown in Fig. 4 (f–h), Na, V, and O elements were uniformly dispersed.

Figure 5a shows the cycling performance of the  $Na_{1.1}V_3O_{7.9}$  samples calcined at different temperatures at 100 mA  $g^{-1}$ . The initial discharge specific capacities of the NVO450, NVO500, and NVO550 samples are 147, 205, and 150 mAh  $g^{-1}$ , respectively, and remained at 31, 195, and 167 mAh  $g^{-1}$  after 150 cycles. The capacity retention rates of the NVO450, NVO500, and NVO550 samples are 21%, 95%,

**Fig. 4** SEM images of the as-prepared  $Na_{1.1}V_3O_{7.9}$  samples calcined at different temperatures for 4 h: (a) 450 °C, (b) 500 °C, and (c) 550 °C. TEM images of the as-prepared  $Na_{1.1}V_3O_{7.9}$  sample calcined at 500 °C for 4 h (d), and the HRTEM image of  $Na_{1.1}V_3O_{7.9}$  (inset in d). The element distribution mapping of the (e) region is (f) Na, (g) V, (h) O, respectively

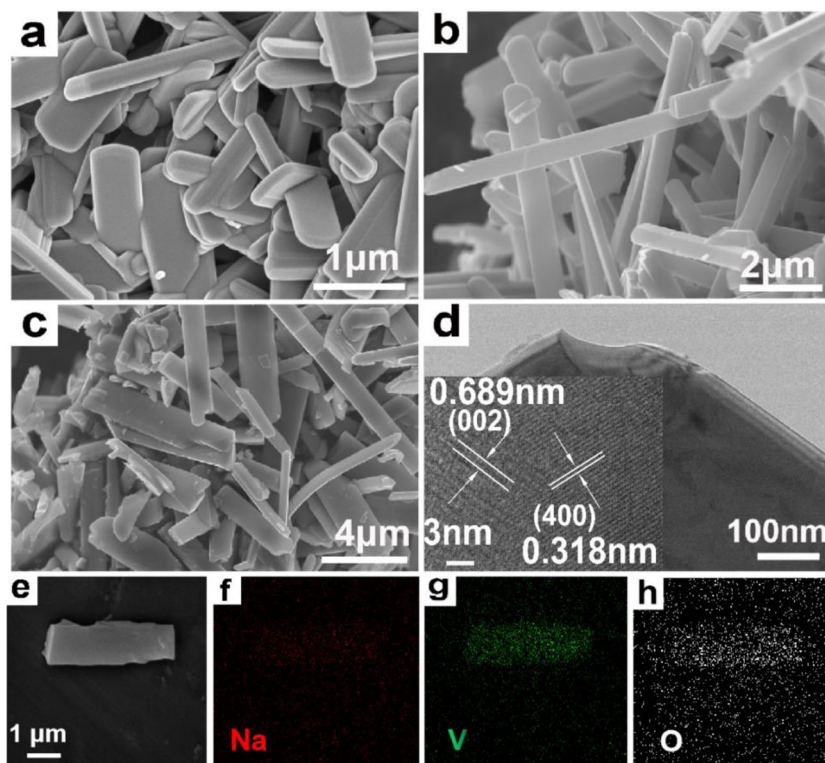
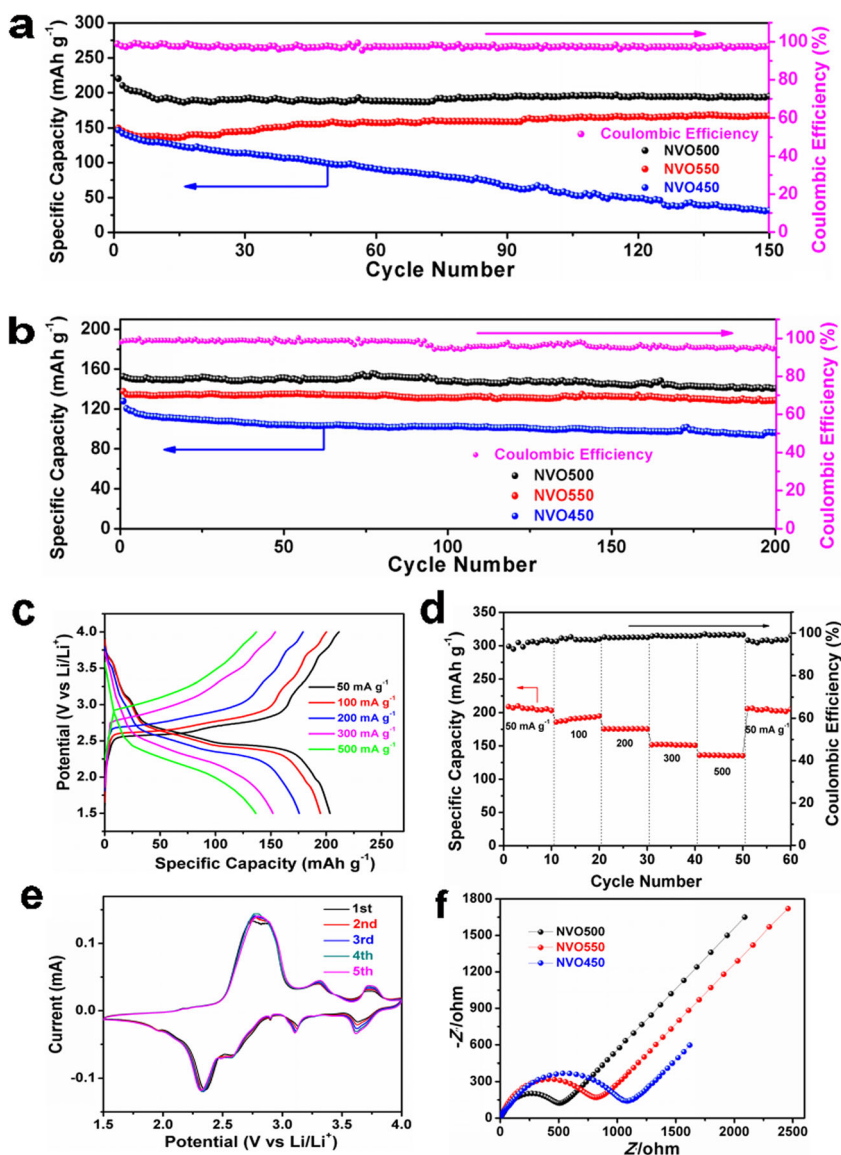




**Fig. 5** Cycling performance of  $\text{Na}_{1.1}\text{V}_3\text{O}_{7.9}$  samples calcined at different temperatures (a)  $100\text{ mA g}^{-1}$  and (b)  $300\text{ mA g}^{-1}$ . (c) Charge-discharge voltage profiles of the NVO500 at current densities varying from  $50\text{ mA g}^{-1}$  to  $500\text{ mA g}^{-1}$ . (d) Rate performance of the NVO500 at various current densities (from  $50\text{ mA g}^{-1}$  to  $500\text{ mA g}^{-1}$ ). (e) The first five successive CV curves of the NVO500 sample at a scan rate of  $0.1\text{ mV s}^{-1}$  from 1.5 V to 4.0 V. (f) Nyquist plots of NVO450, NVO500, and NVO550 samples



and 112%, respectively. Figure 5b shows that the  $\text{Na}_{1.1}\text{V}_3\text{O}_{7.9}$  samples exhibit excellent cycle stability at a current of  $300\text{ mA g}^{-1}$ . After 200 cycles, the discharge specific capacities of the NVO450, NVO500, and NVO550 samples are 96, 141, and 129  $\text{mAh g}^{-1}$ , and the corresponding capacity

retention rates are 75%, 92%, and 94%, respectively. Obviously, the NVO500 sample has the highest specific capacity, and the NVO550 has the best capacity retention, which consistent with the crystallinity and *c*-axis length of the as-prepared  $\text{Na}_{1.1}\text{V}_3\text{O}_{7.9}$  samples at different temperature (Fig.

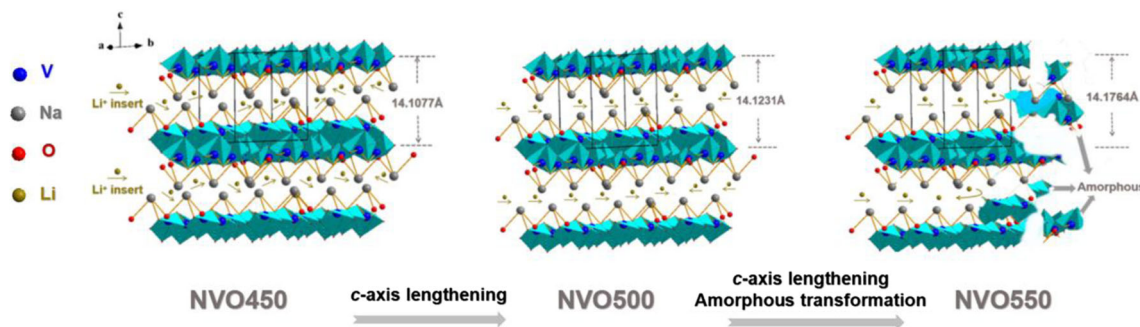


**Fig. 6** Lithium-ion transmission mechanism model diagram

2b), respectively. Figure 5c displays the galvanostatic charge-discharge voltage profiles of the  $\text{Na}_{1.1}\text{V}_3\text{O}_{7.9}$  electrode at various current densities (from  $50 \text{ mA g}^{-1}$  to  $500 \text{ mA g}^{-1}$ ). Three distinct plateaus were observed in each charge-discharge profile, corresponding to the conversion of the vanadium valence state. At high current densities, the sharp drop in the discharge specific capacity of the NVO500 sample is due to the polarization of the electrodes, leading to a reduction in the specific capacity [39]. Figure 5d shows the rated capacity of the NVO500 sample with current densities varying from  $50 \text{ mA g}^{-1}$  to  $500 \text{ mA g}^{-1}$ . The discharge capacity after the 10th cycle is 203.1, 194.7, 175.5, 150.9, and  $135.2 \text{ mAh g}^{-1}$  at 50, 100, 200, 300, and  $500 \text{ mA g}^{-1}$ , respectively. When the current density abruptly returns to  $50 \text{ mA g}^{-1}$ , the capacity recovers to  $204.7 \text{ mAh g}^{-1}$ , reflecting the excellent reversibility and rate capability of the electrode in which made of NVO500 sample. Figure 5e shows the first five successive CV curves of the NVO500 sample at a scan rate of  $0.1 \text{ mV s}^{-1}$  from 1.5 V to 4.0 V. Three cathode peaks observed at 3.6, 3.1, and 2.4 V versus  $\text{Li}/\text{Li}^+$  related to  $\text{Li}^+$  ion intercalation. Also, three anode peaks were retrieved at 2.75, 3.3, and 3.8 V versus  $\text{Li}/\text{Li}^+$ . The position of the cathode/anode peaks is consistent with the discharge/charge plateaus in Fig. 5c. The results show that during the discharging/charging process, the valence state of vanadium continuously changes during the insertion and extraction of  $\text{Li}/\text{Li}^+$  in the electrode  $\text{Na}_{1.1}\text{V}_3\text{O}_{7.9}$ , resulting in a multiple-phase reversible transformation processes [13]. The cyclic voltammogram is similar, indicating the superior reversibility of the  $\text{Na}_{1.1}\text{V}_3\text{O}_{7.9}$  sample. Figure 5f shows the Nyquist plot of different samples calcination at different temperatures. The NVO450, NVO500, and NVO550 samples exhibit a similarly shaped electrochemical impedance spectrogram, where a semicircle and a straight line were detected in the high- and low-frequency regions, respectively. The semicircle of the NVO500 sample is the smallest, which indicates that the sample has low electrochemical reaction resistance but excellent electron conduction and lithium-ion migration rates. The excellent crystallinity of the sample will increase the reaction kinetics, resulting in a better cycle and capacity performance.

The electrochemical performance of the  $\text{Na}_{1.1}\text{V}_3\text{O}_{7.9}$  samples relates to the crystalline structure. The schematic diagram of lithium-ion transmission mechanism was shown in Fig. 6, the *c*-axes of the unit cell become longer with calcination temperature increased, so the layer spacing among the vanadium oxide polyhedron becomes larger. Thus the larger cavity was formed in the *b*-axis direction. Lithium ions are mainly transported and diffused in the monoclinic layer (*b*-axis direction), so the larger layer spacing, more advantageous for lithium-ion transport, the smaller damage of lithium ions to the crystalline structure. Therefore, the larger the layer spacing of the *c*-axis, the higher the sample capacity retention ratio, such as the NVO550 sample, which consistent with Fig. 2b

and Fig. 5a–b. However, due to the amorphous transformation begin at  $550 \text{ }^\circ\text{C}$  (Fig. 2c), the lattice structure was damaged when the calcination temperature raised to  $550 \text{ }^\circ\text{C}$ . The formation of the amorphous state blocked the transport path of lithium ions, so the redox reaction is not complete during the charging/discharging process.

## Conclusion

In summary, the  $\text{Na}_{1.1}\text{V}_3\text{O}_{7.9}$  nanoplates were synthesized by the sol-gel method and then calcined at different temperatures. The crystallinity and the lattice parameter of  $\text{Na}_{1.1}\text{V}_3\text{O}_{7.9}$  cathode materials were calculated by XRD results, the maximum crystallinity  $\text{Na}_{1.1}\text{V}_3\text{O}_{7.9}$  sample was calcined at  $500 \text{ }^\circ\text{C}$ , and the maximum length of *c*-axis was calcined at  $550 \text{ }^\circ\text{C}$ . The DSC test result confirmed that the amorphous transformation begins at  $550 \text{ }^\circ\text{C}$ . The XPS results agree well with the presence of  $\text{Na}_{1.1}\text{V}_3\text{O}_{7.9}$ , which is consistent with the XRD test results. The electrochemical results show that the sample calcined at  $500 \text{ }^\circ\text{C}$  has the highest specific capacity because of the most excellent crystallinity. The lattice parameter and cycling performance results show that the length of *c*-axis increases with the calcination increases, the larger layer spacing of the *c*-axis, the higher sample capacity retention ratio, and then the damage of the lithium-ion to the structure during charging/discharging is smaller, thus maintaining excellent cycle stability.

**Funding information** This work was supported by the Natural Science Foundation of Shandong Province (ZR2018LE003).

## References

1. Shang H, Zuo Z, Yu L, Wang F, He F, Li Y (2018) Low-temperature growth of all-carbon graphdiyne on a silicon anode for high-performance Lithium-ion batteries. *Adv Mater* 30(27):1801459
2. Zhang Q, Chen H, Luo L, Zhao B, Luo H, Han X, Wang J, Wang C, Yang Y, Zhu T, Liu M (2018) Harnessing the concurrent reaction dynamics in active Si and Ge to achieve high performance lithium-ion batteries. *Energy Environ Sci* 11(3):669–681
3. Wu H, Chan G, Choi JW, Ryu I, Yao Y, McDowell MT, Lee SW, Jackson A, Yang Y, Hu L, Cui Y (2012) Stable cycling of double-walled silicon nanotube battery anodes through solid-electrolyte interphase control. *Nat Nanotechnol* 7(5):310–315
4. He X, Luan SZ, Wang L, Wang RY, Du P, Xu YY, Yang HJ, Wang YG, Huang K, Lei M (2019) Facile loading mesoporous  $\text{Co}_3\text{O}_4$  on nitrogen doped carbon matrix as an enhanced oxygen electrode catalyst. *Mater Lett* 244:72–82
5. Huang K, Liu J, Wang L, Chang G, Wang R, Lei M, Wang Y, He Y (2019) Mixed valence  $\text{CoCuMnO}_x$  spinel nanoparticles by sacrificial template method with enhanced ORR performance. *Appl Surf Sci* 487:1145–1151
6. Wang H, Liu R, Li Y, Lü X, Wang Q, Zhao S, Yuan K, Cui Z, Li X, Xin S, Zhang R, Lei M, Lin Z (2018) Durable and efficient hollow

- porous oxide spinel microspheres for oxygen reduction. *Joule* 2(2): 337–348
7. Fergus JW (2010) Recent developments in cathode materials for lithium ion batteries. *J Power Sources* 195(4):939–954
  8. Chen J (2013) Recent Progress in advanced materials for Lithium ion batteries. *Materials* 6(1):156–183
  9. Wang H, Liu S, Ren Y, Wang W, Tang A (2012) Ultrathin  $\text{Na}_{1.08}\text{V}_3\text{O}_8$  nanosheets—a novel cathode material with superior rate capability and cycling stability for Li-ion batteries. *Energy Environ Sci* 5(3):6173–6179
  10. Poizot P, Laruelle S, Grugeon S, Dupont LJ-M, Tarascon (2000) Nano-sized transition-metal oxides as negative-electrode materials for lithium-ion batteries. *Nature* 407(6803):496–499
  11. Fang D, Chen S, Wang X, Bando Y, Golberg D, Zhang S (2018) ZnS Quantum Dots@Multilayered carbon: geological-plate-movement-inspired design for high-energy Li-ion batteries. *J Mater Chem A* 6:8358–8365. <https://doi.org/10.1039/C8TA01667D>
  12. Gao Z, Sun H, Fu L, Ye F, Zhang Y, Luo W, Huang Y (2018) Promises, challenges, and recent progress of inorganic solid-state electrolytes for all-solid-state Lithium batteries. *Adv Mater* 30: 1705702
  13. Liang S, Zhou J, Fang G, Liu J, Tang Y, Li X, Pan A (2013) Ultrathin  $\text{Na}_{1.1}\text{V}_3\text{O}_{7.9}$  nanobelts with superior performance as cathode materials for lithium-ion batteries. *ACS Appl Mater Inter* 5(17): 8704–8709
  14. Pan A, Wu HB, Yu L, Zhu T, Lou XW (2012) Synthesis of hierarchical three-dimensional vanadium oxide microstructures as high-capacity cathode materials for lithium-ion batteries. *ACS Appl Mater Inter* 4(8):3874–3879
  15. Liang X, Gao G, Liu Y, Ge Z, Leng P, Wu G (2017) Carbon nanotubes/vanadium oxide composites as cathode materials for lithium-ion batteries. *J Sol-Gel Sci Techn* 82(1):224–232
  16. Wang Y, Takahashi K, Lee K, Cao G (2006) Nanostructured vanadium oxide electrodes for enhanced lithium-ion intercalation. *Adv Funct Mater* 16(9):1133–1144
  17. Shao J, Li X, Wan Z, Zhang L, Ding Y, Zhang L, Qu Q, Zheng H (2013) Low-cost synthesis of hierarchical  $\text{V}_2\text{O}_5$  microspheres as high-performance cathode for lithium-ion batteries. *ACS Appl Mater Inter* 5(16):7671–7675
  18. Xue L, Savilov SV, Lunin VV, Xia H (2017) Self-standing porous  $\text{LiCoO}_2$  nanosheet arrays as 3D cathodes for flexible Li-ion batteries. *Adv Funct Mater* 1705836
  19. Luo XD, Yin YZ, Yuan M, Zeng W, Lin G, Huang B, Li YW, Xiao SH (2018) High performance composites of spinel  $\text{LiMn}_2\text{O}_4$ /3DG for lithium ion batteries. *RSC Adv* 8(2):877–884
  20. Li Z, Feng X, Mi L, Zheng J, Chen X, Chen W (2018) Hierarchical porous onion-shaped  $\text{LiMn}_2\text{O}_4$  as ultrahigh-rate-cathode material for lithium ion batteries. *Nano Res* 11(8):4038–4048
  21. Deng Y, Zhou Y, Shi Z, Zhou X, Quan X, Chen G (2013) Porous  $\text{LiMn}_2\text{O}_4$  microspheres as durable high power cathode materials for lithium ion batteries. *J Mater Chem A* 1(28):8170–8177
  22. Liu Q, Mao D, Chang C, Huang F (2007) Phase conversion and morphology evolution during hydrothermal preparation of orthorhombic  $\text{LiMnO}_2$ , nanorods for lithium ion battery application. *J Power Sources* 173(1):538–544
  23. Meng Y, Han W, Zhang Z, Zhu F, Zhang Y, Wang D (2017)  $\text{LiFePO}_4$  particles coated with N-doped carbon membrane. *J Nanosci Nanotechnol* 17(3):2000–2005
  24. Eftekhari A (2017)  $\text{LiFePO}_4$ /C nanocomposites for lithium-ion batteries. *J Power Sources* 343:395–411
  25. Tsuda T, Ando N, Matsubara K, Tanabe T, Itagaki K, Soma N, Nakamura S, Hayashi N, Gunji T, Ohsaka T, Matsumoto F (2018) Improvement of high rate performance of a Lithium ion battery composed of laminated  $\text{LiFePO}_4$  cathodes/graphite anodes with porous electrode structure fabricated with a Pico-second pulsed laser. *Electrochim Acta* 291:267–277
  26. Cheng F, Chen J (2011) Transition metal vanadium oxides and vanadate materials for lithium batteries. *J Mater Chem* 21(27): 9841–9848
  27. Li X, Cheng F, Guo B, Chen J (2005) Template-synthesized  $\text{LiCoO}_2$ ,  $\text{LiMn}_2\text{O}_4$ , and  $\text{LiNi}_{0.8}\text{Co}_{0.2}\text{O}_2$  nanotubes as the cathode materials of lithium ion batteries. *J Phys Chem B* 109(29):14017–14024
  28. Wang X, Jia W, Wang L, Huang Y, Guo Y, Sun Y, Jia D, Pang W, Guo Z, Tang X (2016) Simple in situ synthesis of carbon-supported and nanosheet-assembled vanadium oxide for ultra-high rate anode and cathode materials of lithium ion batteries. *J Mater Chem A* 4(36):13907–13915
  29. Jouanneau S, Le GLSA, Verbaere A, Guyomard D, Deschamps M, Lascaud S (2003) New alkaline earth substituted lithium trivanadates: synthesis, characterization and lithium insertion behavior. *J Mater Chem* 13(7):1827–1834
  30. Tang Y, Sun D, Wang H, Huang X, Zhang H, Liu S, Liu Y (2014) Synthesis and electrochemical properties of  $\text{NaV}_3\text{O}_8$  nanoflakes as high-performance cathode for Li-ion battery. *RSC Adv* 4(16): 8328–8334
  31. Cao L, Chen L, Huang Z, Kuang Y, Zhou H, Chen Z (2016)  $\text{NaV}_3\text{O}_8$  nanoplates as a lithium ion battery cathode with superior rate capability and cycle stability. *ChemElectrochem* 3(1):122–129
  32. Yuan S, Liu YB, Xu D, Ma DL, Wang S, Yang XH, Cao ZY, Zhang (2015) Pure single-crystalline  $\text{Na}_{1.1}\text{V}_3\text{O}_{7.9}$  nanobelts as superior cathode materials for rechargeable sodium-ion batteries. *Adv Sci* 2(3):1400018
  33. Gundlach DJ, Royer JE, Park SK, Subramanian S, Jurchescu OD, Hamadani BH, Moad AJ, Kline RJ, Teague LC, Kirillov O, Richter CA, Kushmerick JG, Richter LJ, Parkin SR, Jackson TN, Anthony JE (2008) Contact-induced crystallinity for high-performance soluble acene-based transistors and circuits. *Nat Mater* 7(3):216–221
  34. Zheng Q, Zhang Y, Montazerian M, Gulbitten O, Mauro JC, Zanotto ED, Yue Y (2019) Understanding glass through differential scanning Calorimetry. *Chem Rev* 119(13):7848–7939
  35. Kozhevnikov AV, Anisimov VI, Korotin MA (2007) Calculation of the electronic structure of the vanadium dioxide  $\text{VO}_2$  in the monoclinic low-temperature phase  $M_1$  using the generalized transition state method. *Phys Met Metallogr* 104(3):215–220
  36. Slink WE, Degroot PB (1981) Vanadium-titanium oxide catalysts for oxidation of butene to acetic acid. *J Catal* 68(2):423–432
  37. Horvath AB, Strutz J, Geyer-Lippmann J, Horvath EG (1981) Preparation, properties, and ESCA characterization of vanadium surface compounds on Silicagel. *II Z Anorg Allg Chem* 483(12): 193–204
  38. Bond GC, Zurita JP, Flamerz S (1986) Structure and reactivity of titania-supported oxides. Part 2: characterisation of various vanadium oxide on titania catalysts by x-ray photoelectron spectroscopy. *Appl Catal* 27(2):353–362
  39. Shi Y, Wen L, Li F, Cheng MH (2011) Nanosized  $\text{Li}_4\text{Ti}_5\text{O}_{12}$ /graphene hybrid materials with low polarization for high rate lithium ion batteries. *J Power Sources* 196(20):8610–8617